All-Optical Scalable Spatial Coherent Ising Machine

Marcello Calvanese Strinati,[1,*] Davide Pierangeli,[1,2] and Claudio Conti[1,2,3]

[1]*Physics Department, Sapienza University of Rome, Rome 00185, Italy*
[2]*Institute for Complex Systems, National Research Council (ISC-CNR), Rome 00185, Italy*
[3]*Centro Ricerche Enrico Fermi (CREF), Via Panisperna 89a, Rome 00184, Italy*

Networks of optical oscillators simulating coupled Ising spins have been recently proposed as a heuristic platform to solve hard optimization problems. These networks, called coherent Ising machines (CIMs), exploit the fact that the collective nonlinear dynamics of coupled oscillators can drive the system close to the global minimum of the classical Ising Hamiltonian, encoded in the coupling matrix of the network. To date, realizations of large-scale CIMs have been demonstrated using hybrid optical-electronic setups, where optical oscillators simulating different spins are subject to electronic feedback mechanisms emulating their mutual interaction. While the optical evolution ensures an ultrafast computation, the electronic coupling represents a bottleneck that causes the computational time to severely depend on the system size. Here, we propose an all-optical scalable CIM with fully programmable coupling. Our setup consists of an optical parametric amplifier with a spatial light modulator (SLM) within the parametric cavity. The spin variables are encoded in the binary phases of the optical wave front of the signal beam at different spatial points, defined by the pixels of the SLM. We first discuss how different coupling topologies can be achieved by different configurations of the SLM, and then benchmark our setup with a numerical simulation that mimics the dynamics of the proposed machine. In our proposal, both the spin dynamics and the coupling are fully performed in parallel, paving the way towards the realization of size-independent ultrafast optical hardware for large-scale computation purposes.

I. INTRODUCTION

Solving large-scale optimization problems is extremely useful to several different fields of modern science, with applications ranging from biology to finance and social science [1–5]. These problems often belong to the nondeterministic polynomial (NP-hard) computational complexity class [6]: finding the optimal solution requires computational resources that scale exponentially with the size of the system, making these problems intractable using conventional computer architectures. A tremendous amount of interest has been recently attracted by the development of unconventional computational methods (heuristic solvers) to solve probabilistically, but efficiently, large-scale optimization problems. A key observation behind these heuristic methods is that optimization problems can be mapped onto specific classical Ising models efficiently [7], i.e., in a polynomial (P) time. Solving the specific optimization problem then translates into the NP-hard problem of finding the ground state (GS) of the corresponding Ising Hamiltonian [8].

In recent years, several physical systems have been demonstrated to evolve according to the classical Ising Hamiltonian, therefore providing valuable *ad hoc* platforms to solve the Ising model for large-scale optimization purposes. Remarkable examples include two-component Bose-Einstein condensates [9,10], superconducting circuits [11], trapped ions [12,13], digital computers [14–17], electrical oscillators [18], optoelectronical oscillators [19], polariton condensates [20–22], laser networks [23,24], and coupled optical parametric oscillators (OPOs) [25–38], which are the focus of this work. These networks, called coherent Ising machines (CIMs) exploit the fact that, when driven above the oscillation threshold, a second-order phase transition takes place [39,40]: in the long-time limit, the phase of each OPO takes values 0 or π with respect to the reference phase enforced by the pump. Because of the bistable nature of its phase, an OPO is suitable to simulate a classical Ising spin, and systems of coupled OPOs in proper conditions can simulate the dynamics of coupled Ising spins [29,41,42].

Nowadays, major issues in realizing CIMs for realistic optimization problems involve, on one hand, the physical conditions (e.g., temperature) in which the machine has to operate, and on the other hand, the scalability

*marcello.calvanesestrinati@gmail.com

and the connectivity that these systems can implement. In this respect, photonic systems offer a versatile platform to realize large-scale CIMs with general connectivity, while working at room temperature and being constructed from off-the-shelf components. An implementation of an all-optical CIM with few spins using time-multiplexed OPOs has been reported in Refs. [26,27], where different OPOs are different temporal pulses within a nonlinear cavity, and optical delay lines are used to couple different OPOs. This approach allows the realization of arbitrary coupling topology, but cannot be scaled up to a large number of spins. An all-optical CIM with a large number of spins was reported in Ref. [28], implementing the one-dimensional nearest-neighbor coupling via a Mach-Zehnder interferometer. While this other approach allows the implementation of several spins, the coupling topology was limited to nearest-neighbor coupling. Large-scale CIMs with arbitrary coupling topology have been demonstrated using time-multiplexed OPOs in hybrid optical-electronic systems [32,43], or optoelectronic oscillators [19]: optical signals evolve in time subject to electronic measure and feedback mechanisms to emulate the spin-spin interaction. The optical nature of the setup ensures ultrafast computation. However, the presence of the electronic feedback inherently represents a "bottleneck" that introduces an additional computational time that scales quadratically with the system size [44]. The realization of a scalable fully optical CIM without the hindrance of electronic components is thus highly desirable.

A step towards the realization of an all-optical scalable CIM has been recently made by exploiting spatial degrees of freedom of light [34,45]. This approach relies on the usage of spatial light modulators (SLMs) to encode a spin variable σ_j into the binary phase modulation of the optical field shining the jth pixel of the SLM. An electronic feedback mechanism was also present. To date, a proposal of an all-optical scalable CIM implementing an arbitrary coupling topology is still missing. In this paper, we propose and theoretically validate an all-optical scalable spatial CIM with fully programmable coupling. We first propose two different configurations of the SLM to realize two different classes of coupling, and then estimate the computational performance of our machine by means of a numerical simulation that closely mimics the temporal dynamics of coupled OPOs within a parametric cavity. We find that our proposed setup converges close to the minimum of the Ising Hamiltonian after a computational time that is orders of magnitude smaller compared to existing hybrid electro-optical setups.

This paper is organized as follows. In Sec. II, we discuss the scheme of our proposed setup. In Sec. III, we show our numerical results, and draw our conclusions in Sec. IV.

II. SCHEME OF THE PROPOSED SETUP

The scheme of our machine is shown in Fig. 1(a). We consider an optical parametric cavity with a second-order nonlinear medium ($\chi^{(2)}$ NLM) of length L, shone by a pump laser (green beam) at wavelength λ_p. We take z as the direction of propagation of light. The pump beam within the NLM parametrically amplifies degenerate pairs of signal and idler photons (red beam) at wavelength $\lambda_s = 2\lambda_p$ via spontaneous parametric down-conversion. The spatial configuration of the signal wave front on the x-y plane encodes the amplitudes $\{A_{j,\tau}\}$ of the N OPO fields ($j = 1, \ldots, N$) at round trip number τ. These amplitudes are in general complex, i.e., the phase of the optical field on the x-y plane can take any value. However, the presence of the $\chi^{(2)}$ NLM forces the optical phases to be either 0 or π with respect to the pump phase, making the amplitudes $\{A_{j,\tau}\}$ effectively real, as detailed below.
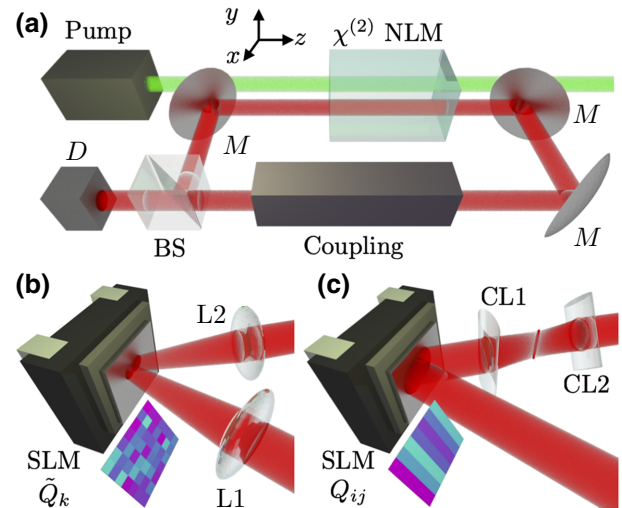

FIG. 1. (a) All-optical spatial CIM. The setup consists of the following: (i) $\chi^{(2)}$ NLM pumped by a laser at wavelength λ_p nonresonant with the cavity mirrors (M), which amplifies the signal at $\lambda_s = 2\lambda_p$, (ii) coupling mechanism, (iii) extraction of the signal by a beam splitter (BS) with reflection and transmission coefficients R_{out} and $T_{\text{out}} = \sqrt{1 - R_{\text{out}}^2}$, respectively, and detection (D). The coupling is implemented using different configurations of the SLM depending on the implemented graph. (b) Circulant graphs: a first lens (L1) transforms the signal in Fourier space, the SLM multiplies the FT of the field by $\tilde{Q}_k$, and a second lens (L2) transforms the modulated field back to real space. (c) General graphs, based on the vector-matrix multiplication scheme. The SLM works in real space, multiplying the incoming field by Q_{ij}. The modulated signal is focused along the y axis by a cylindrical lens (CL1), defocused, and rotated by 90° on the x-y plane by another cylindrical lens (CL2) with 45° rotated optical axis. The pixels in (b) and (c) depict the OPOs encoded on the x-y plane: an amplitude $A_{j,\tau}$ is defined as a single pixel in (b), whereas as a column of M_y pixels in (c).

Different configurations of the SLM with $M_x \times M_y$ pixels realize different couplings between different OPOs, as shown in (b) and (c). In (b), the SLM is placed at the focal plane of a first lens (L1). The discretization of the field in real (and thus momentum) space is enforced by the SLM: different pixels define different OPO amplitudes, thereby defining $N = M_x \times M_y$ different OPOs. Since in commercial SLMs one typically has $M_x, M_y \sim 10^3$, this scheme allows to define $N \sim 10^6$ OPOs. The SLM acts as a programmable matrix with a transmission function $\tilde{Q}_k$, which multiplies at each round trip the Fourier transform (FT) of the incoming OPO amplitudes $\tilde{A}_{k,\tau} = \mathrm{FT}[\{A_{j,\tau}\}]$. A second lens (L2) with the same focal length as L1 transforms the modulated fields $\tilde{Q}_k \tilde{A}_{k,\tau}$ back to real space, yielding the inverse Fourier transform (IFT) of $\tilde{Q}_k \tilde{A}_{k,\tau}$. By convolution theorem, the resulting field on each pixel after the FT-SLM-IFT sequence is $A'_{j,\tau} = \sum_i Q_{i-j+1} A_{i,\tau}$, where Q_j is the IFT of $\tilde{Q}_k$. The output takes the form of a coupled field $A'_{j,\tau} = \sum_i Q_{ij} A_{i,\tau}$, where the coupling matrix $\mathbf{Q}$ has entries $Q_{ij} \equiv Q_{i-j+1}$. This matrix represent a rotationally invariant (or circulant) graph [46], where all nodes are equivalent. Notable examples are the nearest-neighbor Ising chain and the Möbious ladder [26–28,33].

While the coupling scheme in (b) gives the possibility to encode a large number of OPOs, granting a straightforward experimental implementation, it allows the implementation of a limited class of graph. To overcome this issue, we propose in (c) a different scheme for a general coupling matrix $\mathbf{Q}$. This setup is based on the vector-matrix multiplication scheme [47]: the different OPOs are arranged on the x-y plane as different column vectors, such that the signal wave front shines all M_y pixels on a given column of the SLM with a uniform field. The SLM multiplies in real space the vectorized signal with amplitude $A_{j,\tau}$ by Q_{ij}, such that the amplitude at the point (i,j) of the field after the SLM is $Q_{ij} A_{j,\tau}$. A cylindrical lens (CL1) focuses the signal wave front onto a single column along the y axis, whose amplitude at point i is given by $A'_{i,\tau} = \sum_j Q_{ij} A_{j,\tau}$. Propagation in free space defocuses the signal on the x-y plane, obtaining a vectorized signal arranged as a row matrix. Subsequent rotation by $90°$ of the field by a second cylindrical lens (CL2) recovers the structure of the signal as column vectors. Now, each column encodes the amplitude $A'_{j,\tau} = \sum_i Q_{ij} A_{i,\tau}$, i.e., a coupled field with general Q_{ij}. As such, this scheme implements any coupling matrix, but with the drawback that the OPOs need to be redundantly defined over M_y pixels, limiting to $N = M_x$ the number of OPOs in the system.

We stress that the two coupling schemes presented here are fully optical and process all interactions in parallel, without need of electronic feedbacks. Since in our scheme the propagation of the OPOs within the cavity also occurs in parallel, our scheme realizes a size-independent large-scale spatial CIM [44], with critical advantages in terms of scaling and computational time compared to the existing hybrid optical-electronic devices.

In our setup, the binary nature of the phase of each OPO is enforced by the $\chi^{(2)}$ NLM in Fig. 1(a). We inject into the NLM a pump field with spatially uniform wave front that, at each pixel j on the x-y plane, mixes inside the NLM with the signal field. The subsequent dynamics along the z axis, independently at each point, follows the second-order nonlinear wave equation [48] for the degenerate signal field $\{A_{j,\tau}\}$ and pump $\{B_{j,\tau}\}$:

$$\frac{dB_{j,\tau}}{dz} = -\kappa A_{j,\tau}^2 \qquad \frac{dA_{j,\tau}}{dz} = \kappa B_{j,\tau} A_{j,\tau}^*, \qquad (1)$$

where the star denotes complex conjugation. Here, $\kappa = 2\pi \chi^{(2)}/\lambda_s n^2$, where $\chi^{(2)}$ and $n = n(\lambda_s)$ are the nonlinear coefficient and the index of refraction of the NLM, respectively, and $\lambda_s = 2\pi/k_s$. We assume perfect phase matching $2k_s = k_p$, where $k_{s(p)}$ is the wave vector of the signal (pump), which is achieved by tuning the temperature of the NLM to equalize the index of refraction for the signal and pump. To show phase-dependent amplification, we rewrite by omitting j and τ in Eq. (1) $A(z) = u(z) e^{i\phi(z)}$ and $B(z) = u_p(z) e^{i\phi_p(z)}$, where u (u_p) and ϕ (ϕ_p) are the amplitude and phase of the signal (pump), respectively. This allows us to separate the dynamics of the relative phase $\theta = \phi_p - 2\phi$ and of the amplitudes u and u_p in Eq. (1) as

$$\frac{du}{d(\kappa z)} = u u_p \cos(\theta) \qquad \frac{du_p}{d(\kappa z)} = -u^2 \cos(\theta)$$
$$\frac{d\theta}{d(\kappa z)} = \frac{\sin(\theta)}{u_p} \left(u^2 - 2u_p^2 \right). \qquad (2)$$

From Eq. (2), one can see that the evolution of θ has two fixed points (modulo 2π): $\theta = 0$, i.e., $\phi - \phi_p/2 = 0, \pi$ and $\theta = \pi$, i.e., $\phi - \phi_p/2 = \pm\pi/2$, corresponding to two distinct regimes: (i) parametric amplification, where energy is transferred from the pump to the field, and (ii) up-conversion, where energy is converted from the signal to the pump. Focusing on the first case, which is our case of interest, θ flows towards $\theta = 0$, fixing ϕ to be either 0 or π with respect to $\phi_p/2$, thereby manifesting phase-dependent amplification. In terms of the original variables, taking $\phi_p = 0$ (real pump), the evolution along z amplifies the real part of the fields $\mathrm{Re}[A_{j,\tau}]$ and suppresses their imaginary parts $\mathrm{Im}[A_{j,\tau}]$.

III. NUMERICAL RESULTS

We now discuss the experimental realizability of our setup in Fig. 1. We follow Refs. [41,49] using realistic experimental values of the system parameters. Each OPO amplitude $A_{j,\tau}$ evolves into $A_{j,\tau+1}$ after a round trip by undergoing (i) parametric amplification within the NLM

[Eq. (1)], (ii) coupling, and (iii) measurement and losses. We then capture the OPO dynamics by the following map:

$$A_{j,\tau+1} = R_{\text{out}} \sum_l Q_{jl} \, \text{NLM}[A_{l,\tau}]. \tag{3}$$

In Eq. (3), $\text{NLM}[A_{l,\tau}]$ represents the lth OPO amplitude at the exit of the NLM (i.e., for $z = L$), which is computed by integrating Eq. (1) for $z \in [0, L]$ with initial conditions $A_{j,\tau}(z = 0) = A_{j,\tau-1}$ and $B_{j,\tau}(z = 0) = B_0$, where B_0 is the uniform pump amplitude at the entrance of the NLM, which provides the gain. There are two sources of loss: the SLM transmission function **Q**, and measurement and intrinsic loss encoded in R_{out}. The balance between gain and losses during the initial round trips defines the value $B_{0,\text{th}}$ of the oscillation threshold: $B_{0,\text{th}} = -\log[R_{\text{out}}\rho(\mathbf{Q})]/\kappa L$, where $\rho(\mathbf{Q})$ is the spectral radius of **Q**.

We shine the NLM with a pump laser at $\lambda_p = 532$ nm with spot radius $w_0 = 100$ μm. The physical properties of the NLM are encoded in $\chi^{(2)}$, λ_s, and n (determining κ), and L. Here, we use $\chi^{(2)} = 10^{-11}$ m/V, $\lambda_s = 1064$ nm, $n = 2$ ($\kappa \simeq 1.48 \times 10^{-5}$ V^{-1}), and $L = 10$ cm, which defines the characteristic length scale in our simulations. To integrate Eq. (1), we use as characteristic field amplitude $A_0 \simeq 6.77 \times 10^3$ V/m, which yields the numerical rescaled nonlinear constant $\tilde{\kappa} := \kappa z_0 A_0 = 10^{-2}$, and thus integrate Eq. (1) for $z \in [0, 1]$ (in units of L). At $\tau = 0$, the signal consists of white noise with amplitude 10^{-3} A_0.

The SLM transmission function **Q** is written by including self-interaction and off-diagonal coupling terms **J**, which is a real symmetric matrix: $\mathbf{Q} = a\mathbb{1} + b\mathbf{J}$, where $\mathbb{1}$ is the identity matrix. Since the SLM provides phase and amplitude modulation, Q_{ij} is in general a complex number with $|Q_{ij}| < 1$. The lossy nature of the
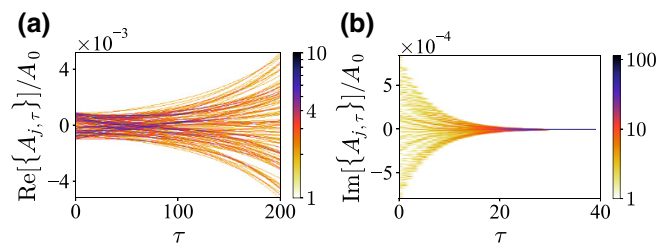

FIG. 2. Histogram of time evolution of the (a) real and (b) imaginary part of the $N = 112$ OPO amplitudes (in units of A_0, see text), computed using Eq. (3), for short times. As evident, the cavity dynamics enhances the real part of the OPO amplitudes and suppresses their imaginary part.

SLM implies $\rho(\mathbf{Q}) < 1$. To benchmark our proof-of-principle machine, we simulate $N = 112$ coupled OPOs and solve the MAX-CUT problem for four undirected graphs for which the optimization problem belongs to different classes of computational complexity (P and NP hard) [41,50]: The Möbius ladder (ML) [51], which is a circulant P graph realized with the scheme in Fig. 1(b), and three NP-hard graphs, specifically the random Erdős-Rényi (ER) and scale-free Barabási-Albert (BA) graphs [52] with approximately 20% edge density, and the random complete (K) graph [53], realized with the scheme in Fig. 1(c). For the ML, the nonzero entries of **J** are $J_{i,i+1} = \alpha$ and $J_{i,i+N/2} = \alpha$, with negative α. For the ER and BA graphs, $J_{ij} = 0, \pm\beta$, where the three values are randomly chosen from the appropriate probability distribution to yield the chosen edge density [52], while for the K graph, $J_{ij} = \pm\gamma$, where the sign is randomly chosen with equal probability. We set $a = 0.96$, $b = 0.04$, $\alpha = -0.2$, and $\beta = 0.05$, and $\gamma = 0.03$, for which $\rho(\mathbf{Q}) \simeq 0.98$ in all cases. In this setup,
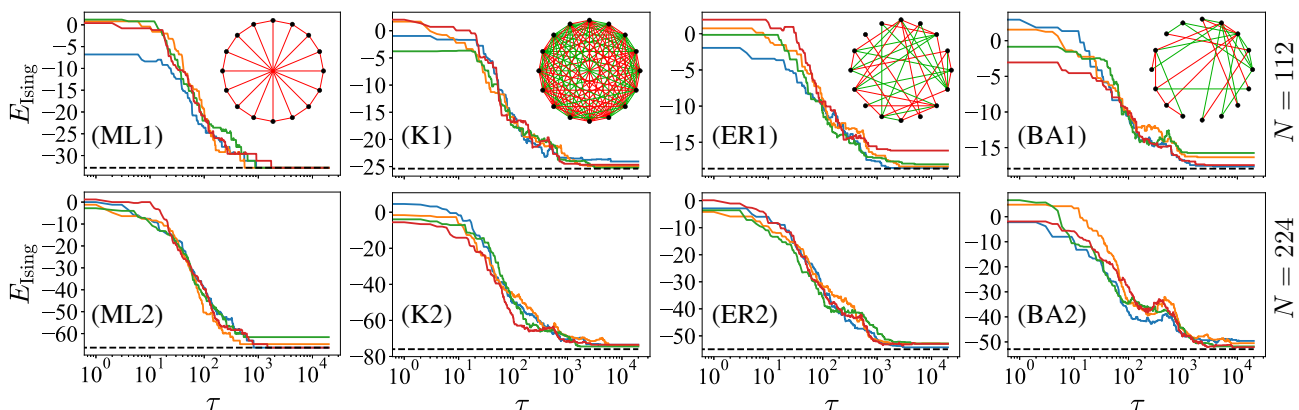

FIG. 3. Ising energy from the OPO phases during the round trips for (ML1),(ML2) Möbius ladder, (K1),(K2) complete graph, (ER1),(ER2) Erdős-Rényi graph, and (BA1),(BA2) Barabási-Albert graph. Upper panels refer to $N = 112$, while lower panels to $N = 224$. Different lines refer to different initial conditions. Horizontal black dashed lines mark the GS energy found by diagonalizing **J** for ML, and the minimal energy found by Metropolis annealing for K, ER, and BA. The insets in the upper panels depict the different connectivities in the four cases (black dots are nodes, and red and green lines depict negative and positive edge weights, respectively), where $N = 16$ is used for illustration purposes only.

TABLE I.　Values of the pump amplitude B_0 at the entrance of the NLM used in the simulation, for the data in Fig. 3.

	ML	K	ER	BA
$N = 112$	$1.2\,B_{0,\text{th}}$	$1.33\,B_{0,\text{th}}$	$1.3\,B_{0,\text{th}}$	$1.3\,B_{0,\text{th}}$
$N = 224$	$1.2\,B_{0,\text{th}}$	$1.36\,B_{0,\text{th}}$	$1.3\,B_{0,\text{th}}$	$1.3\,B_{0,\text{th}}$

by setting $T_{\text{out}} = \sqrt{0.1}$, we obtain threshold pump powers $P_{\text{th}} \sim 200$ mW.

We first show in Fig. 2 the histogram of the time evolution of (a) $\text{Re}[A_{j,\tau}]$, and (b) $\text{Im}[A_{j,\tau}]$, for short times, specifically for ML. As evident, $\text{Re}[A_{j,\tau}]$ is exponentially amplified, whereas $\text{Im}[A_{j,\tau}]$ is instead suppressed. This confirms that the system is correctly in the phase-dependent amplification regime. Next, we simulate the OPO dynamics for the chosen graphs and compute the Ising energy from OPO phase configuration as $E_{\text{Ising}}(\tau) = -(1/2) \sum_{ij} J_{ij} \sigma_i(\tau) \sigma_j(\tau)$, where $\sigma_i(\tau) = \text{sgn}(A_{i,\tau})$ and $\text{sgn}(\cdot)$ is the sign function. We compare the energy for two different values of N, namely $N = 112$ and $N = 224$. The result is shown in Fig. 3. Different panels refer to different graphs and different N as in the labels, using the values of the pump amplitude B_0 at the entrance of the NLM given in Table I. Different solid lines refer to different initial conditions of the fields. The black horizontal lines mark the minimal Ising energy: the P nature of the problem with the ML allows us to find this value exactly by diagonalizing $\mathbf{J}$, selecting the eigenvector with maximal eigenvalue [41]. Instead, for the NP-hard cases of K, ER, and BA, we estimate the minimal value by a Metropolis annealing algorithm. The fact that the steady-state value of E_{Ising} coincides with the exact minimal value for ML, while sometimes it does not for K, ER, and BA, reflects the different computational complexity of the optimization [41,50].

The key result in Fig. 3 is that our system approaches a steady state with energy close to the minimum energy of the corresponding Ising Hamiltonian after about 10^3 round trips, for both values of N. Since in our scheme all OPOs evolve in time in parallel, our device allows to use short cavities (typically $D \sim 1$ m long) that in turn ensures short round trips times $\tau_{\text{RT}} = 2nD/c \sim 10$ ns, independent of N. We then estimate the total computational time as approximately 10 μs. As such, the parallelization of the dynamics allows us to envision orders of magnitude shorter computational time compared to existing CIM realizations [32,33,54,55].

IV. CONCLUSIONS

In conclusion, we propose a fully optical scalable spatial CIM implementing different connectivities. The binary nature of the signal phase at different points on the wave front is enforced by the NLM within the parametric cavity,

and the spatial discretization of the wave front is defined by the SLM within the cavity implementing the spin-spin optical coupling. The number of spins that our system encodes critically depends on the specific configuration of the SLM. To implement a fully programmable CIM, we propose a setup based on the vector-matrix multiplication scheme, where the SLM works in real space of the field. This scheme allows the implementation of any graph, however, limiting the number of spins to $N \sim 10^3$ due to the redundant encoding of the spin variables on the SLM pixels. We then propose an alternative coupling scheme with the SLM working in momentum space of the field, which allows the implementation of a limited class of graphs but it can host $N \sim 10^6$ spins.

The all-optical nature of our machine presents a step towards the realization of large-scale scalable CIMs. First, in our proposal, both the OPO dynamics and their mutual coupling are fully parallelized, which makes the reach for the optimal solution size independent. Second, the parallel encoding of all OPOs allows for short cavity lengths, and thus drastically smaller computational time, compared to state-of-the art realizations with hybrid electronic-optical setups, where the OPOs are arranged as a temporal sequence of pulses and cavity lengths of approximately 1 km are needed. Another advance of our proposal compared to existing realizations is that no measurement is performed during the time evolution to realize the mutual interaction. This makes our machine suitable to study fundamental features of coupled OPOs beyond optimization, like the emergence of robust macroscopic quantum entanglement [56,57].

[1] J. J. Hopfield, Neural networks and physical systems with emergent collective computational abilities, PNAS **79**, 2554 (1982).

[2] M. Gilli, D. Maringer, and E. Schumann, *Numerical Methods and Optimization in Finance* (Elsevier Science, 2011).

[3] Q. Zhang, D. Deng, W. Dai, J. Li, and X. Jin, Optimization of culture conditions for differentiation of melon based on artificial neural network and genetic algorithm, Sci. Rep. **10**, 3524 (2020).

[4] A. Degasperi, D. Fey, and B. N. Kholodenko, Performance of objective functions and optimisation procedures for parameter estimation in system biology models, npj Syst. Biol. Appl. **3**, 20 (2017).

[5] M. Ohzeki, S. Okada, M. Terabe, and S. Taguchi, Optimization of neural networks via finite-value quantum fluctuations, Sci. Rep. **8**, 9950 (2018).

[6] R. M. Karp, in *Complexity of Computer Computations* (1972), p. 85.

[7] A. Lucas, Ising formulations of many NP problems, Front. Phys. **2,** 5 (2014).

[8] F. Barahona, On the computational complexity of Ising spin glass models, J. Phys. A **15,** 3241 (1982).

[9] T. Byrnes, K. Yan, and Y. Yamamoto, Accelerated optimization problem search using Bose-Einstein condensation, New J. Phys. **13,** 113025 (2011).

[10] T. Byrnes, S. Koyama, K. Yan, and Y. Yamamoto, Neural networks using two-component Bose-Einstein condensates, Sci. Rep. **3,** 2531 (2013).

[11] M. W. Johnson, *et al.*, Quantum annealing with manufactured spins, Nature **437,** 194 (2011).

[12] K. Kim, M.-S. Chang, S. Korenblit, R Islam, E. E. Edwards, J. K. Freericks, G.-D. Lin, L.-M. Duan, and C. Monroe, Quantum simulation of frustrated Ising spins with trapped ions, Nature **465,** 590 (2010).

[13] J. W. Britton, B. C. Sawyer, A. C. Keith, C.-C. J. Wang, J. K. Freericks, H. Uys, M. J. Biercuk, and J. J. Bollinger, Engineered two-dimensional Ising interactions in a trapped-ion quantum simulator with hundreds of spins, Nature **484,** 489 (2012).

[14] A. D. King, W. Bernoudy, J. King, A. J Berkley, and T. Lanting, Emulating the coherent Ising machine with a mean-field algorithm, ArXiv:1806.08422 (2018).

[15] E. S. Tiunov, A. E. Ulanov, and A. I. Lvovsky, Annealing by simulating the coherent Ising machine, Opt. Express **27,** 10288 (2019).

[16] H. Goto, K. Tatsumura, and A. R. Dixon, Combinatorial optimization by simulating adiabatic bifurcations in nonlinear Hamiltonian systems, Sci. Adv. **5,** eaav2372 (2019).

[17] K. Tatsumura, M. Yamasaki, and H. Goto, Scaling out ising machines using a multi-chip architecture for simulated bifurcation, Nat. Electron. **4,** 208 (2021).

[18] J. Chou, S. Bramhavar, S. Ghosh, and W. Herzog, Analog coupled oscillator based weighted Ising machine, Sci. Rep. **9,** 14786 (2019).

[19] F. Böhm, G. Verschaffelt, and G. Van der Sande, A poor man's coherent ising machine based on opto-electronic feedback systems for solving optimization problems, Nat. Commun. **10,** 3538 (2019).

[20] N. G. Berloff, M. Silva, K. Kalinin, A. Askitopoulos, J. D. Töpfer, P. Cilibrizzi, W. Langbein, and P. G. Lagoudakis, Realizing the classical XY Hamiltonian in polariton simulators, Nat. Mat. **16,** 1120 (2017).

[21] K. P. Kalinin and N. G. Berloff, Simulating Ising and *n*-State Planar Potts Models and External Fields with Nonequilibrium Condensates, Phys. Rev. Lett. **121,** 235302 (2018).

[22] K. P. Kalinin and N. G. Berloff, Global optimization of spin hamiltonians with gain-dissipative systems, Sci. Rep. **8,** 17791 (2018).

[23] S. Utsunomiya, K. Takata, and Y. Yamamoto, Mapping of Ising models onto injection-locked laser systems, Opt. Express **19,** 18091 (2011).

[24] C. Tradonsky, I. Gershenzon, V. Pal, R. Chriki, A. A. Friesem, O. Raz, and N. Davidson, Rapid laser solver for the phase retrieval problem, Sci. Adv. **5,** 10 (2019).

[25] Z. Wang, A. Marandi, K. Wen, R. L. Byer, and Y. Yamamoto, Coherent Ising machine based on degenerate

[26] A. Marandi, Z. Wang, K. Takata, R. L. Byer, and Y. Yamamoto, Network of time-multiplexed optical parametric oscillators as a coherent Ising machine, Nat. Photonics **8,** 937 (2014).

[27] K. Takata, A. Marandi, R. Hamerly, Y. Haribara, D. Maruo, S. Tamate, H. Sakaguchi, S. Utsonomiya, and Y. Yamamoto, A 16-bit coherent Ising machine for one-dimensional ring and cubic graph problems, Sci. Rep. **6,** 34089 (2016).

[28] T. Inagaki, K. Inaba, R. Hamerly, K. Inoue, Y. Yamamoto, and H. Takesue, Large-scale Ising spin network based on degenerate optical parametric oscillators, Nat. Photonics **10,** 415 (2016).

[29] R. Hamerly, K. Inaba, T. Inagaki, H. Takesue, Y. Yamamoto, and H. Mabuchi, Topological defect formation in 1D and 2D spin chains realized by network of optical parametric oscillators, Int. J. Mod. Phys. B **30,** 1630014 (2016).

[30] W. R. Clements, J. J. Renema, Y. H. Wen, H. M. Chrzanowski, W. S. Kolthammer, and I. A. Walmsley, Gaussian optical Ising machines, Phys. Rev. A **96,** 043850 (2017).

[31] T. Wang and J. Roychowdhury, Oscillator-based Ising machine, ArXiv:1709.08102 (2017).

[32] T. Inagaki, Y. Haribara, K. Igarashi, T. Sonobe, S. Tamate, T. Honjo, A. Marandi, P. L. McMahon, T. Umeki, K. Enbutsu, O. Tadanaga, H. Takenouchi, K. Aihara, K.-i. Kawarabayashi, K. Inoue, S. Utsunomiya, and H. Takesue, A coherent Ising machine for 2000-node optimization problems, Science **354,** 603 (2016).

[33] R. Hamerly, *et al.*, Experimental investigation of performance differences between coherent Ising machines and a quantum annealer, Sci. Adv. **5,** eaau0823 (2019).

[34] D. Pierangeli, G. Marcucci, and C. Conti, Large-Scale Photonic Ising Machine by Spatial Light Modulation, Phys. Rev. Lett. **122,** 213902 (2019).

[35] L. Bello, M. Calvanese Strinati, E. G. Dalla Torre, and A. Pe'er, Persistent Coherent Beating in Coupled Parametric Oscillators, Phys. Rev. Lett. **123,** 083901 (2019).

[36] T. Wang and J. Roychowdhury, in *Unconventional Computation and Natural Computation* (Springer International Publishing, Cham, 2019), p. 232.

[37] Y. Okawachi, M. Yu, J. K. Jang, X. Ji, Y. Zhao, B. Y. Kim, M. Lipson, and A. L. Gaeta, Demonstration of chip-based coupled degenerate optical parametric oscillators for realizing a nanophotonic spin-glass, Nat. Commun. **11,** 4119 (2020).

[38] D. Pierangeli, G. Marcucci, and C. Conti, Adiabatic evolution on a spatial-photonic Ising machine, Optica **7,** 1535 (2020).

[39] E. Goto, The parametron, a digital computing element which utilizes parametric oscillation, Proc. IRE **47,** 1304 (1959).

[40] J. Woo and R. Landauer, Fluctuations in a parametrically excited subharmonic oscillator, IEEE J. Quantum Electron **QE-7,** 435 (1971).

[41] M. Calvanese Strinati, L. Bello, E. G. Dalla Torre, and A. Pe'er, Can Nonlinear Parametric Oscillators Solve

Random Ising Models?, Phys. Rev. Lett. **126,** 143901 (2021).

[42] M. Erementchouk, A. Shukla, and P. Mazumder, Computational capabilities of nonlinear oscillator networks, ArXiv:2105.07591 (2021).

[43] Y. Haribara, S. Utsunomiya, and Y. Yamamoto, in *Principles and Methods of Quantum Information Technologies*, edited by Yoshihisa Yamamoto and Kouichi Semba (Springer Japan, Tokyo, 2016), p. 251.

[44] D. Pierangeli, M. Rafayelyan, C. Conti, and S. Gigan, Scalable Spin-Glass Optical Simulator, Phys. Rev. Appl. **15,** 034087 (2021).

[45] S. Kumar, H. Zhang, and Y.-P. Huang, Large-scale Ising emulation with four body interaction and all-to-all connections, Comm. Phys. **3,** 108 (2020).

[46] P. J. Davis, *Circulant Matrices, Chelsea Publishing Series* (Chelsea, 1994).

[47] J. Spall, X. Guo, T. D. Barrett, and A. I. Lvovsky, Fully reconfigurable coherent optical vector–matrix multiplication, Opt. Lett. **45,** 5752 (2020).

[48] R. W. Boyd, *Nonlinear Optics* (Elsevier Science, 2008).

[49] M. Calvanese Strinati, I. Aharonovich, S. Ben-Ami, E. G. Dalla Torre, L. Bello, and A. Pe'er, Coherent dynamics in frustrated coupled parametric oscillators, New J. Phys. **22,** 085005 (2020).

[50] K. P. Kalinin and N. G. Berloff, Complexity continuum within Ising formulation of NP problems, ArXiv:2008. 00466 (2020).

[51] R. K. Guy and F. Harary, On the Möbius ladders, Canad. Math. Bull. **10,** 493 (1967).

[52] R. Albert and A.-L. Barabási, Statistical mechanics of complex networks, Rev. Mod. Phys. **74,** 47 (2002).

[53] D. Gries and F. B. Schneider, *A Logical Approach to Discrete Math* (Springer-Verlag, 1993).

[54] Y. Haribara, H. Ishikawa, S. Utsunomiya, K. Aihara, and Y. Yamamoto, Performance evaluation of coherent Ising machines against classical neural networks, Quantum Sci. Technol. **2,** 044002 (2017).

[55] Y. Yamamoto, K. Aihara, T. Leleu, K. Kawarabayashi, S. Kako, M. Fejer, K. Inoue, and H. Takesue, Coherent Ising machines-optical neural networks operating at the quantum limit, njp Quantum Inf. **3,** 49 (2017).

[56] S. Kiesewetter and P. D. Drummond, Weighted phase-space simulations of feedback coherent Ising machines, ArXiv:2105.04190 (2021).

[57] Z.-Y. Zhou, C. Gneiting, J. Q. You, and F. Nori, Generating and detecting entangled cat states in dissipatively coupled degenerate optical parametric oscillators, Phys. Rev. A **104,** 013715 (2021).